RSC Advances

PAPER

View Article Online
View Journal | View Issue

Cite this: *RSC Adv.*, 2025, **15**, 18114

Two-dimensional Janus α-Au_2XY (X, Y = S/Se/Te) semiconductors with favourable band gaps and high carrier mobilities predicted by first-principles investigations†

Nguyen T. Hiep, [ab] Quach K. Quang,[c] Mai T. V. Nhan,[c] Khanh V. Hoang,[d] Cuong Q. Nguyen, [ab] Bui D. Hoi *[e] and Nguyen N. Hieu [ab]

In this work, two-dimensional Janus α-Au_2XY (X, Y = S/Se/Te) monolayers are designed and their structural stabilities and fundamental properties are investigated using first-principle calculations. We find that the three α-Au_2SSe, α-Au_2STe, and α-Au_2SeTe structures have high energetic, thermodynamic and mechanical stabilities, indicating that experimental fabrication is feasible. In addition, the proposed systems have anisotropic Young's modulus and Poisson's ratio values. According to the electronic structure calculations, the α-Au_2XY monolayers are indirect semiconductors with appropriate band gaps for sunlight absorption of 1.06 to 1.33 eV at the Perdew–Burke–Ernzerhof level. The calculation results from the Heyd–Scuseria–Ernzerhof method for the α-Au_2XY monolayers also show indirect band gap semiconductor behavior. Moreover, we utilize the deformation potential technique to analyze the electron and hole mobilities of the α-Au_2XY materials to determine their transport properties. Interestingly, α-Au_2SSe shows an impressive hole carrier mobility of 6258.42 $cm^2\ V^{-1}\ s^{-1}$ along the *y*-axis. α-Au_2STe and α-Au_2SeTe also have high electron mobilities (μ_e) of 642.21/584.96 $cm^2\ V^{-1}\ s^{-1}$ and 676.56/760.39 $cm^2\ V^{-1}\ s^{-1}$ in the *x*/*y* directions, respectively. In view of the remarkable electronic and transport properties, the α-Au_2XY materials are expected to be promising Janus materials for next-generation optical, electronic, and photovoltaic devices.

Received 24th February 2025
Accepted 13th May 2025

DOI: 10.1039/d5ra01319d

rsc.li/rsc-advances

1 Introduction

In order to meet the demand for innovative materials in advanced technologies, many scientists around the world have been researching and developing new materials for next-generation devices. In the last two decades, two-dimensional (2D) nanomaterials have attracted much attention due to their unique structures with outstanding electronic,[1,2] magnetic,[3,4] catalytic,[5,6] optoelectronic,[7,8] thermodynamic,[9,10] and photovoltaic[11] properties, which are superior to those of their bulk counterparts. The 2D material library has expanded since the discovery of graphene with the appearance of antinonene,[12] phosphorene,[13] transition-metal chalcogenides,[14] transition-metal oxides,[15,16] and MXenes.[17] In particular, 2D Janus monolayers are emerging as novel 2D materials with remarkable properties derived from their asymmetric structures.[18–20] In studies of 2D Janus materials, investigations using density functional theory (DFT) have proven to be an effective method and have proposed many novel Janus structures with intriguing physical properties.[21,22] In addition to theoretical studies, 2D Janus MoSSe materials were first successfully synthesized using the chemical vapor deposition technique.[23] This has led to Janus materials undergoing more intensive study.

For applications in electronics, photonics, and photovoltaics, the band-gap energy and carrier mobility are very important factors affecting the material properties. The potential materials require favorable band gaps for solar spectrum absorption, as well as good charge transport with high carrier mobility. As a result, research teams have concentrated on exploring new Janus materials with these intriguing properties. For example, based on first-principles simulations, Bouziani *et al.* found Janus $SnGeS_2$ and Sn_2SSe to be potential absorbers with promising optical and electronic properties for solar energy conversion systems. They are indirect semiconductors with moderate band-gap energies of 1.61 eV for $SnGeS_2$ and

[a]*Institute of Research and Development, Duy Tan University, Da Nang 550000, Vietnam. E-mail: hieunn@duytan.edu.vn*

[b]*Faculty of Natural Sciences, Duy Tan University, Da Nang 550000, Vietnam*

[c]*Division of Physics, School of Education, Dong Thap University, Cao Lanh 870000, Vietnam*

[d]*Phenikaa Institute for Advanced Study (PIAS), Phenikaa University, Hanoi 12116, Vietnam*

[e]*Faculty of Physics, University of Education, Hue University, Hue 530000, Vietnam. E-mail: buidinhhoi@hueuni.edu.vn*

† Electronic supplementary information (ESI) available. See DOI: https://doi.org/10.1039/d5ra01319d

1.60 eV for Sn_2SSe. Moreover, the $SnGeS_2$ and Sn_2SSe monolayers showed a maximum optical conductivity of 4513 Ω^{-1} cm^{-1} with low reflectivity of less than 38.5% in the visible spectrum. In addition, the monolayers also had a large absorption coefficient of more than 49.7 μm^{-1}. Consequently, the single-junction solar cells based on these monolayers reached high photovoltaic efficiencies of 27.47% for $SnGeS_2$ and 28.12% for Sn_2SSe.[24] Ge and co-workers used density functional theory to investigate the structural and electronic properties of PtX_2 and Janus PtXY monolayers with X/Y = S/Se/Te. They confirmed that these monolayers were stable and highly flexible from the phonon spectra, elastic constants, and the Young's modulus results. At the Perdew–Burke–Ernzerhof level, PtX_2 and Janus PtXY had indirect band gaps varying from 0.76 to 1.81 eV. The electronic properties of these monolayers were tunable under applied strains. They observed that with increasing tensile strain, there was a presence of an indirect band gap to a quasi-direct band-gap transition. These results revealed potential semiconductors for optoelectronic and nanoelectronic applications.[25] Based on $MoSi_2N_4$, Ding and co-workers designed 2D Janus $XMoSiN_2$ semiconductors with X = S/Se/Te. From the calculation results, the $XMoSiN_2$ exhibited metal-like electrical conductivity due to its extremely high carrier mobility, which reached 4640 cm^2 V^{-1} s^{-1}.[26] Yin *et al.* studied the fundamental behaviors of Janus MoSSe/GaN heterostructures using first-principles calculations. They reported that the proposed structures showed a high hole mobility of 3951.2 cm^2 V^{-1} s^{-1} and electron mobility of 281.28 cm^2 V^{-1} s^{-1}. Specifically, stacking modes of the heterostructure and Janus structure could adjust the carrier mobility. In addition, the deformation potential contributed to the varied electron and hole mobilities, and the elastic moduli and equivalent mass also influenced the carrier mobility of the heterostructure.[27] Recently, by using first-principles investigations, Janus group-III chalcogenide MX monolayers with M = Ga/In and X = S/Se were reported to exhibit semiconducting behavior with optimal band gaps of 1.295 eV for Se–In–Ga–S and 1.752 eV for S–In–Ga–Se. Notably, type I and II band alignment transitions could be realized through surface termination at the interface and various stacking configurations because of the interlayer interaction. The heterostructures based on these MX monolayers possessed a maximum power conversion efficiency of 16.2%.[28]

2D gold chalcogenides are predicted to hold great promise for applications in nanoelectronics, thanks to their exceptional physical and mechanical properties. The carrier mobility in gold-based 2D structures is very high,[29] making them suitable for applications in nanoelectronics. Also, gold chalcogenides have been explored for a wide range of applications in various fields, including catalysis,[30] and photoluminescence.[31] In particular, gold chalcogenides have been successfully fabricated experimentally.[32] Herein, we theoretically design 2D Janus α-Au_2XY (X; Y = S/Se/Te) monolayers and explore their fundamental characteristics using first-principles calculations. After optimizing the crystal α-Au_2XY structures, we elucidate their stabilities by calculating cohesive energies and elastic constants, and by performing *ab initio* molecular dynamics simulations. The Young's modulus and Poisson's ratio of the three proposed systems are also examined. Additionally, the electronic structures of the α-Au_2SSe, α-Au_2STe, and α-Au_2SeTe monolayers are investigated by using both the Perdew–Burke–Ernzerhof and Heyd–Scuseria–Ernzerhof methods. We also calculate the work functions of the α-Au_2XY configurations to indicate the ability of electrons to leave the material's surfaces. Notably, we use the deformation potential technique to analyze the carrier mobilities and related parameters of the α-Au_2XY for their transport properties.

2 Computational methods

With the Vienna *ab initio* simulation program,[33,34] we apply the projector augmented wave (PAW) approach[35,36] to construct the crystal structures and explore the properties of α-Au_2XY (X; Y = S/Se/Te) monolayers based on density functional theory (DFT). To verify thermal stability, a canonical ensemble is used for the *ab initio* molecular dynamics (AIMD) simulation with a canonical ensemble at room temperature (300 K). The exchange–correlation potential is estimated from the Perdew–Burke–Ernzerhof (PBE) functional using a generalized gradient approximation (GGA).[37] In addition, the band gap energy is computed from the electronic band structures using the Heyd–Scuseria–Ernzerhof (HSE06)[38] hybrid functional. To integrate a supercell's Brillouin zone (BZ), a 12 × 12 × 1 *k* grid is used with the Monkhorst technique.[39] Along the *z*-axis, a vacuum space of 30 Å is applied to prevent interactions between the periodic slabs. We use a cut-off of 650 eV for the kinetic energy.[35,36] The density functional perturbation theory (DFPT) approach is employed to estimate the elastic constants based on the strain–stress connection. The convergence of the Hellmann–Feynman force and the total energy criteria are determined to be 10^{-3} eV $Å^{-1}$ and 10^{-6} eV, respectively. To correct the dipole moment resulting from the asymmetric Janus structures, we utilize the dipole layer technique for electrostatic potential computations. For the carrier mobilities, the deformation potential (DP) technique is used to analyze the transport characteristics.[40]

3 Results and discussion

3.1 Structural parameters and stability

We initially build the geometric configuration of the α-Au_2SSe, α-Au_2STe, and α-Au_2SeTe monolayers. As shown in Fig. 1(a), the black rectangle primitive cell of the three α-Au_2XY structures contains four atoms including two Au atoms, one X atom, and one Y atom. In this case, one Au atom bonds with one X atom and one Y atom, and the second Au atom tetra-coordinates with two X atoms and two Y atoms. The atomic positions of the proposed Janus structures are shown in Table S1 of the ESI.† It should also be mentioned that several 2D Janus materials have also been successfully fabricated experimentally, including Janus MoSSe[23,41] and PtSSe.[42] Table 1 summarizes the optimized lattice parameters of the proposed configurations. The calculated lattice constants *a*/*b* of α-Au_2SSe, α-Au_2STe, and α-Au_2SeTe are, respectively, 3.58/6.02, 3.72/6.14, and 3.81/6.08 Å. Along the

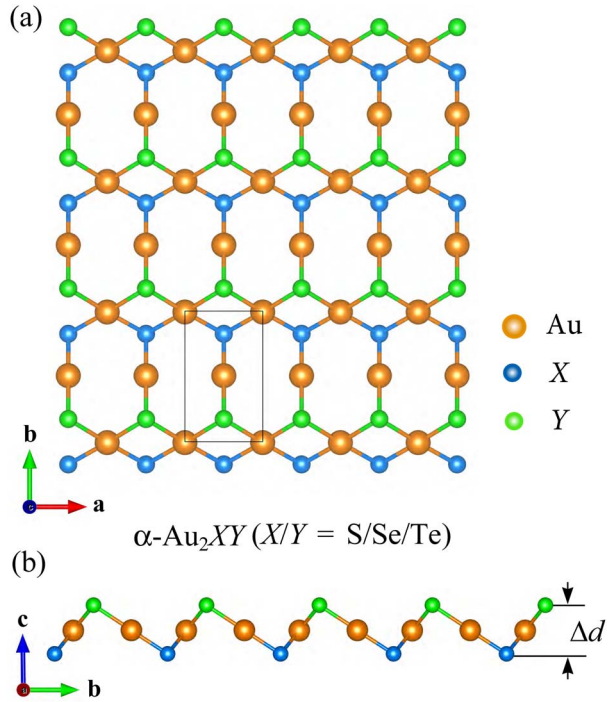

Fig. 1 Crystal structure of α-Au_2XY systems with top (a) and side (b) views.

z-axis, the α-Au_2XY structures are formed from three atomic layers of X–Au–Y, as depicted in Fig. 1(b). Their monolayer thickness Δd increases from 2.59 Å for α-Au_2SSe to 2.73 and 2.90 Å for, respectively, α-Au_2STe and α-Au_2SeTe monolayers. This is due to the increasing of the bond lengths between Au and X/Y atoms. Since the α-Au_2SSe has the lowest $d_{Au\text{-}X}/d_{Au\text{-}Y}$ of 2.39/2.49 Å, the α-Au_2STe and α-Au_2SeTe monolayers have the higher $d_{Au\text{-}X}/d_{Au\text{-}Y}$ values of 2.43/2.64 Å and 2.54/2.65 Å, respectively. Accordingly, the monolayer thickness and the increased bond lengths of the α-Au_2XY are in good agreement with the increasing of the atomic radii of X and Y from 1.84 Å for the S atom to 1.98 Å for Se and 2.21 Å for the Te atom.[43,44] Compared with their corresponding symmetric structures, *i.e.*, α-AuX, we find that the Janus α-Au_2SSe has a lattice constant a = 3.58 Å, which is larger than that of α-AuS (3.54 Å)[29] but smaller than that of α-AuSe (3.65 Å).[45] In contrast, the lattice constant b of Janus α-Au_2SSe (6.02 Å) is smaller than that of α-AuS (6.18 Å)[29] but larger than that of α-AuSe (5.95 Å).[45] It is also noted that the 2D α-AuSe has been experimentally fabricated for a long time and its lattice constants are a = 3.690(7), b = 8.355(2), and c = 3.663(1) Å.[46]

Next, to indicate the bonding strength for the energetic stability of the materials, the cohesive energy (E_{coh}) of the α-Au_2XY systems are estimated as follows:

$$E_{coh} = \frac{(2E_{Au} + E_X + E_Y) - E_{tot}}{N_{tot}}, \quad (1)$$

where E_{Au}, E_X, and E_Y correspond to the energy of Au, X, and Y atoms, respectively. E_{tot} and N_{tot} are the total energy and total atom number (N_{tot} = 4) in the unit cell. The obtained negative E_{coh} values of the α-Au_2XY monolayers range from −3.75 to −3.52 eV per atom as listed in Table 1. The higher E_{coh} of the α-Au_2SSe compared with the α-Au_2STe and α-Au_2SeTe is correlated to its shorter bond lengths, resulting in the stronger chemical bonds. Thus, the α-Au_2SSe system is more energetically stable among these three studied monolayers. In general, the α-Au_2XY materials have comparable E_{coh} values with those of reported 2D Sb_2Se_2Te,[47] $BInSe_2$,[48] and $MoSi_2P_4$ (ref. 49) materials, implying the high feasibility to fabricate the α-Au_2XY materials experimentally.

We also evaluate the dynamic stability of the proposed structures by calculating their phonon spectra. Dynamic stability is indicated by the presence of only real phonon frequencies (where the square of the vibrational frequency is positive). Conversely, the appearance of imaginary frequencies in the phonon spectrum signifies a lack of restoring force against atomic displacements, implying structural instability. The phonon spectra of the Janus α-Au_2XY materials are shown in Fig. 2(a). It is demonstrated that there are no imaginary frequencies in the phonon spectra of all three proposed structures, implying that the they are dynamically stable.

AIMD simulations are also conducted to evaluate the thermal stability of the α-Au_2XY configurations. The dependence of total energy with simulation time (7 ps) at 500 K of the α-Au_2SSe, α-Au_2STe, and α-Au_2SeTe monolayers are illustrated in Fig. 2(b). During the AIMD simulations, we only observe small energy fluctuations, meaning the total energies of three monolayers are quite stable. From the inset atomic structures after the simulations, the bonding of the α-Au_2XY structures is well maintained without any reconstruction/fracture, suggesting that the three α-Au_2XY systems are thermodynamically stable.

3.2 Mechanical properties

Moreover, we analyse the mechanical properties of the α-Au_2XY monolayers by determining their elastic constants of C_{11}, C_{12}, C_{22}, and C_{66}. To estimate the elastic constants, we apply a strain between −1.5 to 1.5% to the x/y-axis. The elastic constant values

Table 1 Lattice constants a and b (Å), monolayer thickness Δd (Å), bond lengths of $d_{Au\text{-}X}$ and $d_{Au\text{-}Y}$ (Å), cohesive energy E_{coh} (eV per atom), elastic constants C_{11}, C_{12}, C_{22}, C_{66} (N m^{-1}), band gaps E_g (eV) from PBE and HSE06 methods of the α-Au_2XY monolayers. The calculated work function Φ_1 (Φ_2) on the X (Y) side and the vacuum level difference $\Delta\Phi$ of α-Au_2XY monolayers in eV

	a	b	Δd	$d_{Au\text{-}X}$	$d_{Au\text{-}Y}$	E_{coh}	C_{11}	C_{12}	C_{22}	C_{66}	E_g^{PBE}	E_g^{HSE06}	Φ_1	Φ_2	$\Delta\Phi$
α-Au_2SSe	3.58	6.02	2.59	2.39	2.49	−3.75	38.91	2.81	9.57	3.68	1.33	1.99	6.21	5.78	0.43
α-Au_2STe	3.72	6.14	2.73	2.43	2.64	−3.64	36.12	2.20	7.38	2.29	1.09	1.63	6.10	5.19	0.91
α-Au_2SeTe	3.81	6.08	2.90	2.54	2.65	−3.52	36.88	1.39	5.77	1.33	1.06	1.60	5.66	5.08	0.58

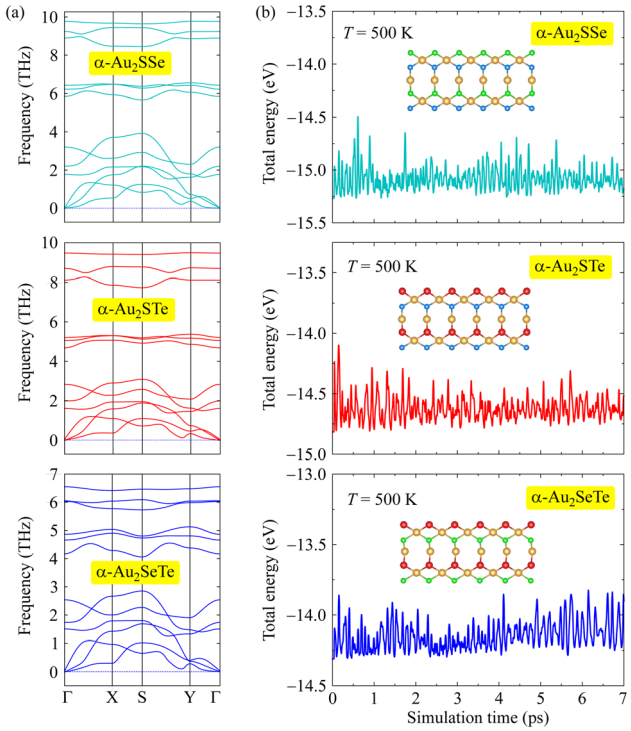

Fig. 2 Phonon spectra (a) and simulation time-dependence of the total energy from AIMD calculation at 500 K of Janus α-Au_2XY monolayers. Insets in (b) correspond to the α-Au_2XY lattices after the AIMD simulation.

are then obtained by fitting the applied strains with the varying energies.[50] As shown in Table 1, all four obtained elastic constants are positive. The α-Au_2SSe has higher elastic constant values than those of the other α-Au_2STe and α-Au_2SeTe monolayers. This may relate to the larger electronegativity of S (2.58) and Se (2.55) atoms compared with the Te atom (2.1), resulting in a larger elastic modulus with shorter bond lengths. The C_{11} and C_{12} values vary from 36.88 to 38.91 N m^{-1} and 1.39 to 2.81 N m^{-1}, respectively. Thus, the elastic constants of the α-Au_2XY monolayers obey the Born and Huang criterion of $C_{11} - C_{12} > 0$ and $C_{66} > 0$ for mechanical stability.[51,52] This confirms that the α-Au_2SSe, α-Au_2STe, and α-Au_2SeTe materials are mechanically stable for laboratory fabrication.

From the attained elastic constants, the material stiffness and deformation are evaluated by analyzing the Young's modulus $Y_{2D}(\theta)$ and Poisson's ratio $\nu_{2D}(\theta)$ with polar coordinates using the following equations:[52,53]

$$Y_{2D}(\theta) = \frac{C_{11}C_{22} - C_{12}^2}{C_{11}\sin^4\theta + C_{22}\cos^4\theta - (2C_{12} - H)\sin^2\theta\cos^2\theta}, \quad (2)$$

$$\nu_{2D}(\theta) = \frac{C_{12}(\sin^4\theta + \cos^4\theta) - (C_{11} + C_{22} - H)\sin^2\theta\cos^2\theta}{C_{11}\sin^4\theta + C_{22}\cos^4\theta - (2C_{12} - H)\sin^2\theta\cos^2\theta}, \quad (3)$$

where θ indicates the angle relative to the x-axis and $H = (C_{11}C_{22} - C_{12}^2)/C_{66}$.

The Young's modulus values of the α-Au_2XY configurations are highly anisotropic, as shown by the Young's modulus diagram in Fig. 3(a). All three monolayers have the maximum $Y_{2D}(\theta)$ values at $\theta = 0°$ of 38.09 N m^{-1} for α-Au_2SSe, 35.46 N m^{-1} for α-Au_2STe, and 36.54 N m^{-1} for α-Au_2SeTe. Thus, at $\theta = 0°$, the α-Au_2SSe structure is slightly stiffer than the other two structures. This is consistent with its having the largest cohesive energy as mentioned above. After reaching the maximum, the $Y_{2D}(\theta)$ values steadily decrease and reach much lower values of 9.37, 7.25, and 5.71 N m^{-1} for α-Au_2SSe, α-Au_2STe, and α-Au_2SeTe, respectively. These attained $Y_{2D}(\theta)$ values of α-Au_2XY are smaller than those of some other 2D materials, such as Al_2SO ($Y_{2D} = 90.23$ N m^{-1}),[54] MoS_2 (123 N m^{-1}),[55] and graphene (336 N m^{-1}).[56] Thus the three proposed α-Au_2XY structures have quite similar anisotropic Young's modulus values and high mechanical flexibility.

The polar Poisson's ratio diagrams of the α-Au_2XY materials are illustrated in Fig. 3(b). It is easy to observe that the Poisson's ratio diagrams of the three monolayers also have quite similar shapes with anisotropic behaviors. At $\theta = 0°$, the $\nu_{2D}(\theta)$ values of α-Au_2SSe, α-Au_2STe, and α-Au_2SeTe are, respectively, 0.29, 0.30, and 0.24. The Poisson's ratios of the three monolayers spatially increase and reach the maximum values at about $\theta = 30°$, then they steadily decrease to the minimum $\nu_{2D}(\theta)$ values at $\theta = 90°$. The maximum $\nu_{2D}(\theta)$ of values of 0.44 for α-Au_2SS, 0.54 for α-Au_2STe, and 0.65 for α-Au_2SeTe at about $\theta = 30°$are higher than

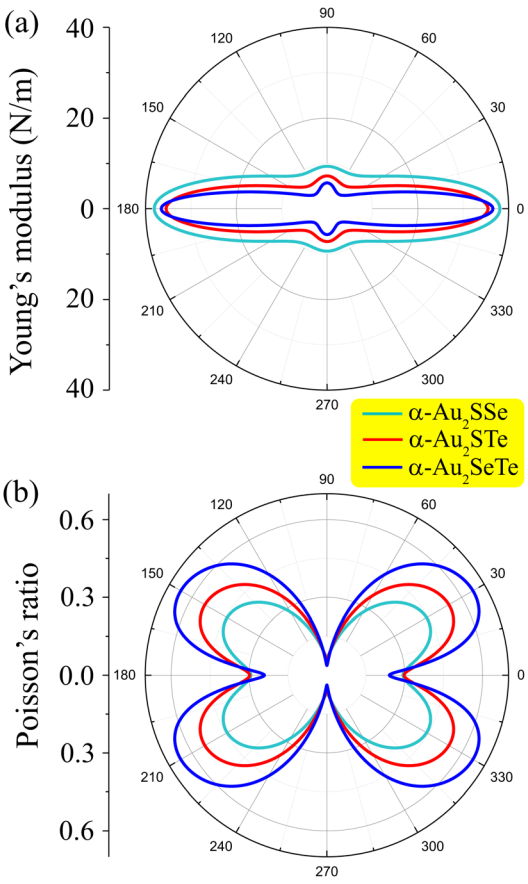

Fig. 3 (a) Young's modulus and (b) Poisson's ratio diagrams as a function of the in-plane angle θ of α-Au_2XY monolayers.

the Poisson's ratios of other reported materials, such as 2D PtSeTe ($\nu_{2D} = 0.27$),[25] ZrSeTe ($\nu_{2D} = 0.26$),[57] and Sn_2PAs ($\nu_{2D} = 0.24$).[54]

3.3 Electronic properties

In this section, we study the electronic properties of the α-Au_2XY monolayers by calculating their band structures in the BZ along the Γ–X–S–Y–Γ point path. As displayed in Fig. 4, the three α-Au_2SSe, α-Au_2STe, and α-Au_2SeTe systems are found to have semiconductor characteristics. At the PBE level, the α-Au_2SSe exhibits an indirect band gap of 1.33 eV with the conduction-band minimum (CBM) located between the Γ–X-points, and the valence-band maximum (VBM) located at the S-point. Meanwhile, the α-Au_2STe and α-Au_2SeTe structures have lower indirect band gaps of 1.09 and 1.06 eV, with the CBM and VBM located at the Γ–X/S–Y and Γ–X/Y point paths, respectively.

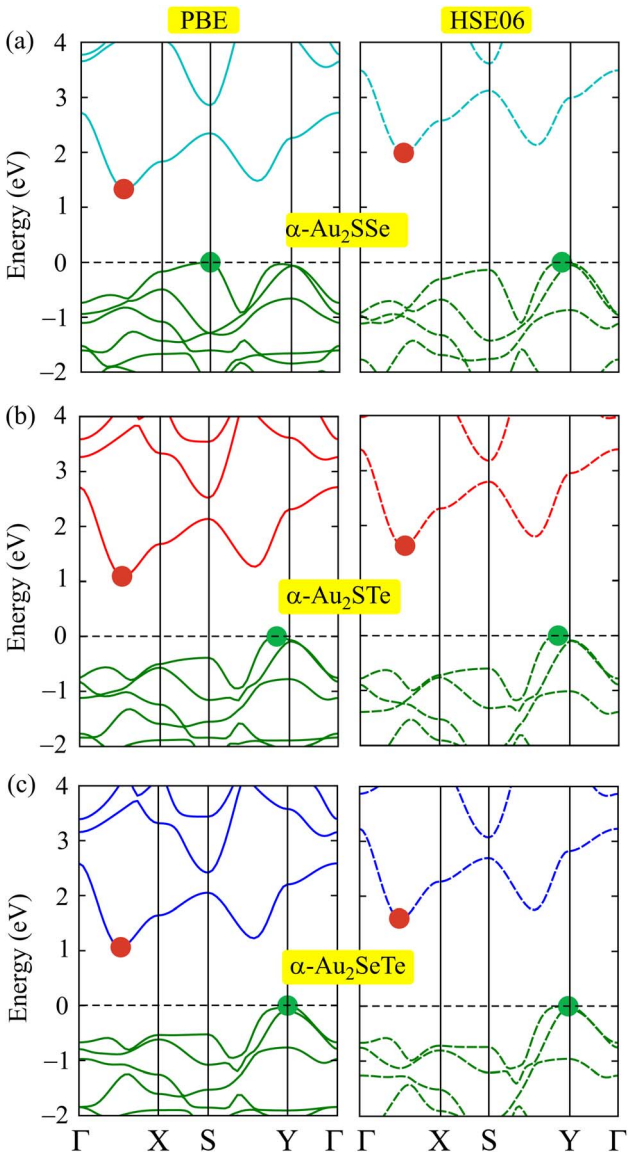

Fig. 4 Electronic band structures from PBE and HSE06 approaches of (a) α-Au_2SSe, (b) α-Au_2STe, and (c) α-Au_2SeTe systems.

These obtained band gaps of about 1.0 eV for the α-Au_2XY materials are appropriate for sunlight absorption, making them promising semiconductors for photovoltaic systems. PBE systematically underestimates the band gap because it suffers from self-interaction errors and delocalization errors, and it lacks the correct treatment of exchange interactions. Meanwhile, HSE06 partially corrects these problems by mixing in a fraction of exact Hartree–Fock exchange with the PBE exchange–correlation energy, and by screening the Coulomb potential to focus on short-range interactions. The calculated results for the band structures of α-Au_2XY using the HSE06 functional are also shown in Fig. 4. Similar to the results from the PBE approach, the band structures from the HSE06 method also show indirect semiconductor behavior for all three α-Au_2XY monolayers. The calculated band gaps at the HSE06 level for α-Au_2SSe, α-Au_2STe, and α-Au_2SeTe are 1.99, 1.63, and 1.60 eV, respectively, as presented in Table 1.

Furthermore, to determine the required energy for the electrons to escape the material's surface, we estimate their work functions Φ from the Fermi (E_F) and vacuum (E_{vac}) levels according to the following formula:

$$\Phi = E_{vac} - E_F. \quad (4)$$

A dipole adjustment is necessary for electrostatic potential calculations due to the existence of intrinsic electric fields caused by the asymmetry of Janus α-Au_2XY structures.[58] The electrostatic potential diagrams of the α-Au_2XY configurations are depicted in Fig. 5. All three monolayers have a work function Φ_1 on the X side that is higher than the work function Φ_2 on the Y side. This can be related to the higher electronegativity of the X atoms compared with the Y atoms. As tabulated in Table 1, the Φ_1/Φ_2 values decrease from 6.21/5.78 eV for α-Au_2SSe to 6.10/5.19 eV for α-Au_2STe, and 5.66/5.08 eV for the α-Au_2SeTe monolayer. It is more difficult for the electrons to escape from the surface at higher energy. According to these obtained Φ_1/Φ_2 values, the calculated electrostatic potential difference $\Delta\Phi$ of the α-Au_2XY materials are 0.43, 0.91, and 0.58 eV for α-Au_2SSe, α-Au_2STe, and α-Au_2SeTe, respectively.

3.4 Transport properties

Finally, the transport properties of the α-Au_2XY monolayers are explored to elucidate their potential applications in the electronic fields. The carrier mobilities μ_{2D} are estimated based on the deformation potential method, which can be expressed as follows:[40,59]

$$\mu_{2D} = \frac{e\hbar^3 C_{2D}}{k_B T m^* \overline{m} E_d^2}, \quad (5)$$

where $\overline{m} = \sqrt{m_x^* m_y^*}$ denotes the average effective mass. k_B and $\hbar$, respectively, relate to the Boltzmann and reduced Planck constants. E_d is the deformation potential. e refers to the elementary charge. C_{2D} indicates the elastic modulus and T is room temperature of 300K. Before getting μ_{2D}, we need to calculate m^*, a significant parameter that strongly affects the mobility of carriers. m^* can be expressed by the following calculation:

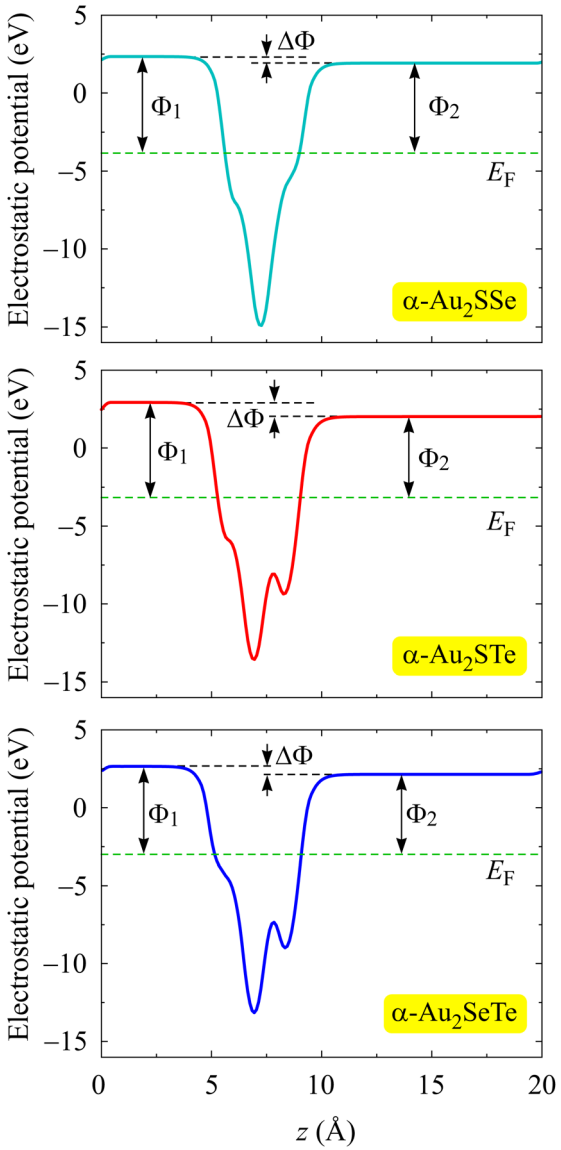

Fig. 5 Electrostatic potentials of α-Au_2XY monolayers with the dashed green line indicating the Fermi level.

$$\frac{1}{m^*} = \frac{1}{\hbar^2}\left|\frac{\partial^2 E(k)}{\partial k^2}\right|, \tag{6}$$

where $E(k)$ denotes the energy in the CBM/VBM regions of the k wave vector. From this equation, we can see that the band diagrams close to the band edges have influences on m^*. The small $\partial^2 E(k)/\partial k^2$ value corresponding to the flat band edge region results in a high effective mass. The attained m^* values for the α-Au_2XY monolayers are presented in Table 2. It is noted that in the cases of Janus α-Au_2XY monolayers, the CBM is located between the Γ and X points in the Brillouin zone, as shown in Fig. 4. The effective masses m_x^* and m_y^* are defined relative to that band's extremum point. m_x^* is the effective mass along the Γ–X direction, which is the direction along the conduction band valley (*i.e.*, longitudinal effective mass) and m_y^* is the effective mass in the direction perpendicular to Γ–X, *i.e.*, the Γ–Y direction (transverse effective mass). Generally, the electron effective masses (m_e^*) along the x direction are quite low, ranging from 0.21 to 0.26 m_0, which are lower than the m_e^* values in the y direction and the hole effective masses (m_h^*). The α-Au_2XY monolayers have quite high m_h^* values in the x direction of 4.70 m_0 for α-Au_2SSe, 1.07 m_0 for α-Au_2STe, and 1.16 m_0 for α-Au_2SeTe. This may affect their μ_{2D} values because the high effective masses lead to the low response of carriers, resulting in lower carrier mobilities.

For the calculation of the elastic modulus C_{2D} and DP constant E_d, we apply uniaxial strains ($\varepsilon_{uni}^{x/y}$) ranging from −0.4 to 0.4% along the two in-plane axes, and estimate the C_{2D} and E_d by using the following equations:

$$E_d = \frac{\Delta E_{edge}}{\varepsilon_{uni}}, \tag{7}$$

$$C_{2D} = \frac{1}{\Omega_0}\frac{\partial^2 E_{tot}}{\partial \varepsilon_{uni}{}^2}, \tag{8}$$

where ε_{uni} denotes the applied strains in the transport directions. Ω_0 and E_{tot}, respectively, correspond to the unit cell area and total energy. ΔE_{edge} refers to the changing energies of the CBM/VBM.

As shown in Fig. 6(a), the α-Au_2STe and α-Au_2SeTe monolayers have quite different band-edge energies along the two in-plane directions under various applied strains from −0.4 to 0.4%. Whereas, the band-edge changing energies of the α-Au_2SSe and the CBM/VBM positions of the α-Au_2XY monolayers are not much different along the x/y directions. E_d and C_{2D} can be obtained from the fitting curves of the positions and energies of the band edges with the band-edge energies/positions under applied strains.[59,60] It can be seen that the calculated C_{2D} and E_d values in Table 2 are quite different along the two in-plane transport directions. α-Au_2SSe has the highest C_{2D} of 78.06

Table 2 Effective masses m^* (in units of the free electron mass: m_0), 2D elastic modulus C_{2D} (Nm^{-1}), DP constants E_d (eV), and carrier mobilities μ ($cm^2\ V^{-1}\ s^{-1}$) of an electron and a hole along the two in-plane transport directions of α-Au_2XY materials

		m_x^*	m_y^*	$C_{2D}{}^x$	$C_{2D}{}^y$	$E_d{}^x$	$E_d{}^y$	μ_x	μ_y
Electron	α-Au_2SSe	0.26	0.57	78.06	73.14	−6.20	−3.75	431.55	504.17
	α-Au_2STe	0.21	0.48	68.89	64.40	−5.85	−3.92	642.21	584.96
	α-Au_2SeTe	0.24	0.38	69.99	56.77	−5.51	−3.72	676.56	760.39
Hole	α-Au_2SSe	4.70	0.26	78.06	73.14	−6.88	−0.93	6.75	6258.42
	α-Au_2TSe	1.07	0.59	68.89	64.40	−2.44	−4.44	289.51	148.23
	α-Au_2SeTe	1.16	0.63	69.99	56.77	−7.46	−3.21	26.97	217.60

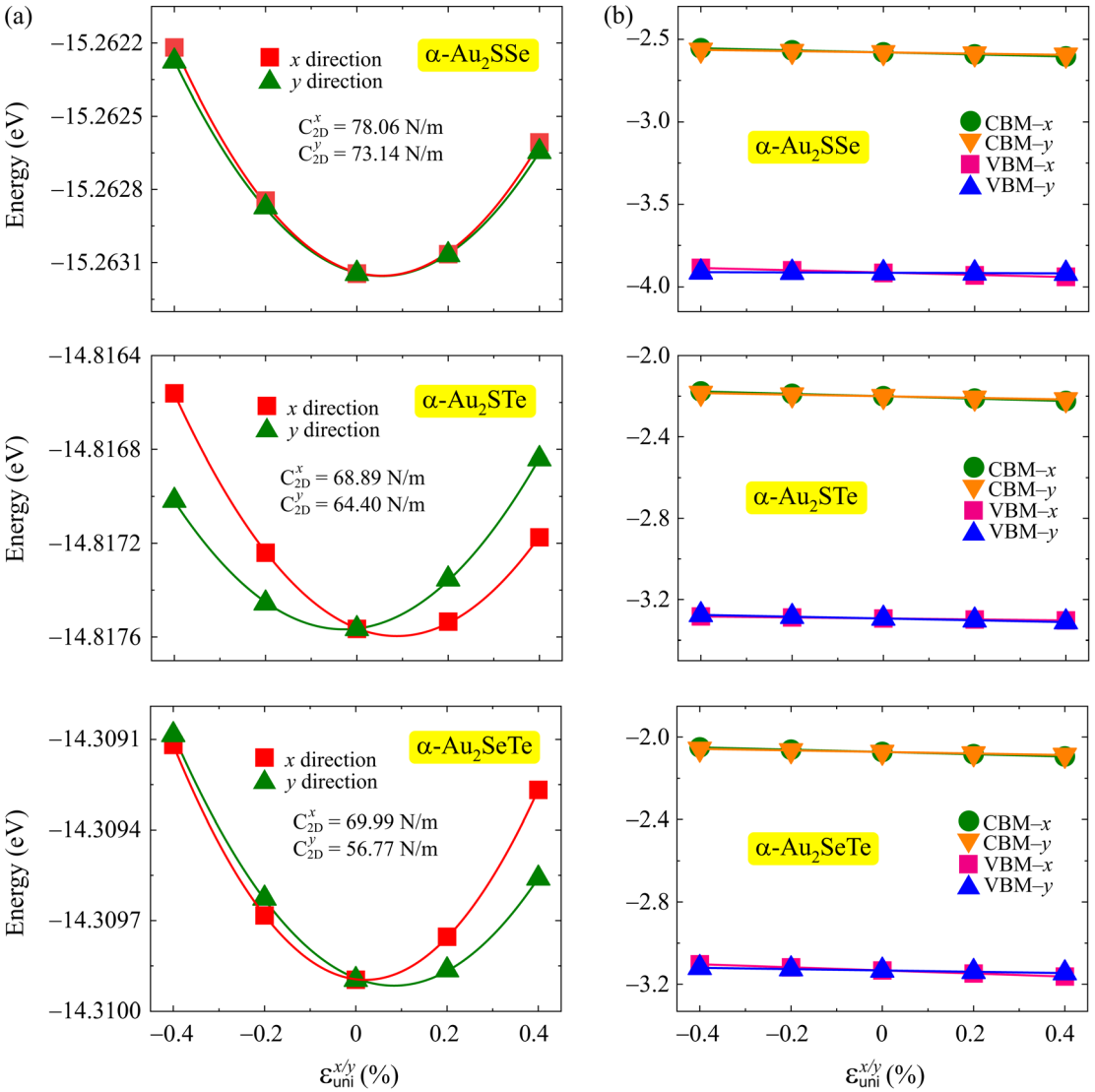

Fig. 6 (a) The shifting of the total energies and (b) CBM/VBM positions with the uniaxial strain of α-Au_2XY systems along the two in-plane axes. The solid lines are fitting curves.

Nm^{-1} in the x direction, and the α-Au_2SeTe exhibits the lowest C_{2D} of 56.77 Nm^{-1} in the y direction. Some other reported 2D materials, such as Ga_2SX_2,[61] Ga_2Te_3,[58] and $STiSiAs_2$ (ref. 62) also exhibited anisotropic E_d values. Similarly, the highest E_d of −0.93 eV is obtained for α-Au_2SSe and the lowest E_d of −7.46 eV is obtained for α-Au_2SeTe. This directional anisotropy of the elastic modulus and DP constants may cause the anisotropic carrier mobilities of the α-Au_2XY monolayers.

Consequently, the carrier mobilities μ_{2D} of the α-Au_2XY monolayers can be estimated from the obtained C_{2D}, E_d, and m^* values according to eqn (5). As expected from the high hole effective masses in the x direction, all three α-Au_2XY monolayers exhibit quite low hole mobilities (μ_h) of 6.75 to 289.51 $cm^2\ V^{-1}\ s^{-1}$ along the x-axis. However, α-Au_2SSe shows the highest μ_h values of 6258.42 $cm^2\ V^{-1}\ s^{-1}$ along the y-axis. α-Au_2STe and α-Au_2SeTe also have high electron mobilities (μ_e) of 642.21/584.96 $cm^2\ V^{-1}\ s^{-1}$ and 676.56/760.39 $cm^2\ V^{-1}\ s^{-1}$ along the x/y axes, respectively. These attained electron mobilities of the α-Au_2STe and α-Au_2SeTe systems are comparable with the μ_e values of the reported 2D Si_2STe (μ_e = 530.98 $cm^2\ V^{-1}\ s^{-1}$),[63] ZrSSe (μ_e = 682.14 $cm^2\ V^{-1}\ s^{-1}$),[64] and $WSiP_3H$ (μ_e = 403.21 $cm^2\ V^{-1}\ s^{-1}$) materials.[65] Meanwhile, the hole mobility value of the α-Au_2SSe monolayer along the y-axis is much higher. This indicates that the α-Au_2SSe, α-Au_2STe, and α-Au_2SeTe materials are potential candidates for electronic transport. It is clear that in the DP theory, the carrier mobility depends not only on the mass but also on the DP constant and C_{2D}. Therefore, despite the small effective masses of the α-Au_2XY materials, their carrier mobilities are not very high because they have large DP constants (absolute value) and small elastic moduli.

4 Conclusions

By using first-principles simulations, we have designed and explored the fundamental characteristics of the Janus α-Au_2XY monolayers. We find that the monolayer thickness and bond

lengths of the proposed α-Au_2SSe, α-Au_2STe, and α-Au_2SeTe configurations increase with the increasing of the X and Y atomic radii. From the AIMD simulations, the α-Au_2XY structures are thermodynamically stable without any reconstruction/fracture during the heating at 300 K. In addition, the cohesive energy and elastic constant results confirm the high energetic and mechanical stabilities for experimental fabrications of the α-Au_2SSe, α-Au_2STe, and α-Au_2SeTe materials. Anisotropic behavior is found for the Young's modulus and Poisson's ratio of the proposed systems. According to the electronic structure calculations, the α-Au_2XY monolayers are indirect semiconductors with appropriate band gaps for sunlight absorption of 1.06 to 1.33 eV at the PBE level. The calculation results from the HSE06 approach of the α-Au_2XY monolayers also indicate indirect band gap semiconductor behavior. Notably, the transport properties of the α-Au_2XY configurations are explored by calculating their carrier mobilities and related parameters. The α-Au_2SSe, α-Au_2STe, and α-Au_2SeTe materials have anisotropic carrier mobilities. Interestingly, α-Au_2SSe shows an impressive hole carrier mobility of 6258.42 $cm^2 V^{-1} s^{-1}$ along the *y*-axis. α-Au_2STe and α-Au_2SeTe also have high electron mobilities (μ_e) of 642.21/584.96 $cm^2 V^{-1} s^{-1}$ and 676.56/760.39 $cm^2 V^{-1} s^{-1}$ in the *x*/*y* axes, respectively. From the remarkable electronic and transport properties, α-Au_2XY structures are expected to be promising Janus materials for next-generation optical, electronic, and photovoltaic devices.

Data availability

All data that support the findings of this study are included within the article.

Conflicts of interest

There are no conflicts of interest to declare.

Acknowledgements

Khanh V Hoang acknowledges Phenikaa University for providing HPC computational resources.

References

1 H. R. Banjade, J. Pan and Q. Yan, *Phys. Rev. Mater.*, 2021, **5**, 014005.
2 N. D. Hien, D. V. Lu and L. C. Nhan, *Nanoscale Adv.*, 2023, **5**, 4546–4552.
3 D. Muoi, N. N. Hieu, C. V. Nguyen, B. D. Hoi, H. V. Nguyen, N. D. Hien, N. A. Poklonski, S. S. Kubakaddi and H. V. Phuc, *Phys. Rev. B*, 2020, **101**, 205408.
4 C. Zhang, Y. Nie, S. Sanvito and A. Du, *Nano Lett.*, 2019, **19**, 1366–1370.
5 Y. Zhu, L. Peng, Z. Fang, C. Yan, X. Zhang and G. Yu, *Adv. Mater.*, 2018, **30**, 1706347.
6 N. N. Som and P. K. Jha, *Int. J. Hydrogen Energy*, 2020, **45**, 23920.
7 M. J. Varjovi, M. E. Kilic and E. Durgun, *Phys. Rev. Mater.*, 2023, **7**, 034002.
8 M. Zhao, Y. Hao, C. Zhang, R. Zhai, B. Liu, W. Liu, C. Wang, S. H. M. Jafri, A. Razaq, R. Papadakis, J. Liu, X. Ye, X. Zheng and H. Li, *Crystals*, 2022, **12**, 1087.
9 Y.-S. Lan, Q. Lu, C.-E. Hu, X.-R. Chen and Q.-F. Chen, *Appl. Phys. A*, 2019, **125**, 33.
10 N. Wang, C. Shen, Z. Sun, H. Xiao, H. Zhang, Z. Yin and L. Qiao, *ACS Appl. Energy Mater.*, 2022, **5**, 2564–2572.
11 F. Zhang, J. Qiu, H. Guo, L. Wu, B. Zhu, K. Zheng, H. Li, Z. Wang, X. Chen and J. Yu, *Nanoscale*, 2021, **13**, 15611–15623.
12 D. Singh, S. K. Gupta, Y. Sonvane and I. Lukačević, *J. Mater. Chem. C*, 2016, **4**, 6386–6390.
13 V. Chaudhary, P. Neugebauer, O. Mounkachi, S. Lahbabi and A. E. Fatimy, *2D Mater.*, 2022, **9**, 032001.
14 Y. Dahiya, M. Hariram, M. Kumar, A. Jain and D. Sarkar, *Coord. Chem. Rev.*, 2022, **451**, 214265.
15 F. Song, L. Bai, A. Moysiadou, S. Lee, C. Hu, L. Liardet and X. Hu, *J. Am. Chem. Soc.*, 2018, **140**, 7748–7759.
16 M. J. Varjovi, M. Yagmurcukardes, F. M. Peeters and E. Durgun, *Phys. Rev. B*, 2021, **103**, 195438.
17 Y. Gogotsi and B. Anasori, *ACS Nano*, 2019, **13**, 8491–8494.
18 J. Schmeink, J. Osterfeld, O. Kharsah, S. Sleziona and M. Schleberger, *npj 2D Mater. Appl.*, 2024, **8**, 67.
19 V. Q. Nha, N. Q. San, H. T. T. Linh, T. V. Vu and N. D. Hien, *Nanoscale Adv.*, 2025, **7**, 2301–2308.
20 T. V. Vu, A. Kartamyshev, M. D. Nguyen, K. D. Pham, T. T. Trinh, N. P. Nhuan and N. D. Hien, *Mater. Sci. Semicond.Process.*, 2024, **181**, 108590.
21 T. V. Vu, H. V. Phuc, A. I. Kartamyshev and N. N. Hieu, *Appl. Phys. Lett.*, 2023, **122**, 061601.
22 T. V. Vu, V. T. T. Vi, H. V. Phuc, A. I. Kartamyshev and N. N. Hieu, *Phys. Rev. B*, 2021, **104**, 115410.
23 A.-Y. Lu, H. Zhu, J. Xiao, C.-P. Chuu, Y. Han, M.-H. Chiu, C.-C. Cheng, C.-W. Yang, K.-H. Wei, Y. Yang, Y. Wang, D. Sokaras, D. Nordlund, P. Yang, D. A. Muller, M.-Y. Chou, X. Zhang and L.-J. Li, *Nat. Nanotechnol.*, 2017, **12**, 744.
24 I. Bouziani, M. Kibbou, Z. Haman, N. Khossossi, I. Essaoudi, A. Ainane and R. Ahuja, *Phys. E*, 2021, **134**, 114900.
25 X. Ge, X. Zhou, D. Sun and X. Chen, *ACS Omega*, 2023, **8**, 5715–5721.
26 C.-H. Ding, Z.-F. Duan, Z.-K. Ding, H. Pan, J. Wang, W.-H. Xiao, W.-P. Liu, Q.-Q. Li, N.-N. Luo, J. Zeng, W. Ren, L.-M. Tang and K.-Q. Chen, *Europhys. Lett.*, 2023, **143**, 16002.
27 W.-J. Yin, X.-L. Zeng, B. Wen, Q.-X. Ge, Y. Xu, G. Teobaldi and L.-M. Liu, *Front. Phys.*, 2021, **16**, 33501.
28 Y. Zhao, Q. Tan, H. Li, Z. Li, Y. Wang and L. Ma, *Sci. Rep.*, 2024, **14**, 10698.
29 Q. Wu, W. W. Xu, D. Lin, J. Wang and X. C. Zeng, *J. Phys. Chem. Lett.*, 2019, **10**, 3773–3778.
30 R. Meyer, C. Lemire, S. K. Shaikhutdinov and H. J. Freund, *Gold Bull.*, 2004, **37**, 72–124.
31 F. K.-W. Hau, T. K.-M. Lee, E. C.-C. Cheng, V. K.-M. Au and V. W.-W. Yam, *Proc. Natl. Acad. Sci. U.S.A.*, 2014, **111**, 15900–15905.

32 G. Palyanova, Y. Mikhlin, V. Zinina, K. Kokh, Y. Seryotkin and T. Zhuravkova, *J. Phys. Chem. Solids*, 2020, **138**, 109276.
33 G. Kresse and J. Furthmüller, *Phys. Rev. B:Condens. Matter Mater. Phys.*, 1996, **54**, 11169–11186.
34 G. Kresse and J. Furthmüller, *Comput. Mater. Sci.*, 1996, **6**, 15–50.
35 P. E. Blöchl, *Phys. Rev. B:Condens. Matter Mater. Phys.*, 1994, **50**, 17953.
36 G. Kresse and D. Joubert, *Phys. Rev. B:Condens. Matter Mater. Phys.*, 1999, **59**, 1758–1775.
37 J. P. Perdew, K. Burke and M. Ernzerhof, *Phys. Rev. Lett.*, 1996, **77**, 3865.
38 J. Heyd, G. E. Scuseria and M. Ernzerhof, *J. Chem. Phys.*, 2003, **118**, 8207.
39 H. J. Monkhorst and J. D. Pack, *Phys. Rev. B*, 1976, **13**, 5188–5192.
40 J. Bardeen and W. Shockley, *Phys. Rev.*, 1950, **80**, 72.
41 J. Zhang, S. Jia, I. Kholmanov, L. Dong, D. Er, W. Chen, H. Guo, Z. Jin, V. B. Shenoy, L. Shi and J. Lou, *ACS Nano*, 2017, **11**, 8192–8198.
42 R. Sant, M. Gay, A. Marty, S. Lisi, R. Harrabi, C. Vergnaud, M. T. Dau, X. Weng, J. Coraux, N. Gauthier, O. Renault, G. Renaud and M. Jamet, *npj 2D Mater. Appl.*, 2020, **4**, 41.
43 D. Ghosh and R. Biswas, *Int. J. Mol. Sci.*, 2003, **4**, 379–407.
44 S. Gao, T. Broux, S. Fujii, C. Tassel, K. Yamamoto, Y. Xiao, I. Oikawa, H. Takamura, H. Ubukata, Y. Watanabe, K. Fujii, M. Yashima, A. Kuwabara, Y. Uchimoto and H. Kageyama, *Nat. Commun.*, 2021, **12**, 201.
45 C. Tang, L. Zhang, C. Zhang, J. MacLeod, K. K. Ostrikov and A. Du, *Nanoscale Horiz.*, 2020, **5**, 366–371.
46 A. Rabenau and H. Schulz, *J. Less-Common Met.*, 1976, **48**, 89–101.
47 L. Zhang, Y. Gu and A. Du, *ACS Omega*, 2021, **6**, 31919–31925.
48 D. Bezzerga, E.-A. Haidar, C. Stampfl, A. Mir and M. Sahnoun, *Nanoscale Adv.*, 2023, **5**, 1425–1432.
49 Y. Liu, C. Shao, W. Yu, Q. Gui, J. Robertson and Y. Guo, *Appl. Phys. Lett.*, 2022, **121**, 244105.
50 K.-A. N. Duerloo, M. T. Ong and E. J. Reed, *J. Phys. Chem. Lett.*, 2012, **3**, 2871–2876.
51 R. C. Andrew, R. E. Mapasha, A. M. Ukpong and N. Chetty, *Phys. Rev. B:Condens. Matter Mater. Phys.*, 2012, **85**, 125428.
52 N. T. Hung, A. R. T. Nugraha and R. Saito, *J. Phys. D: Appl. Phys.*, 2018, **51**, 075306.
53 P. Xiang, S. Sharma, Z. M. Wang, J. Wu and U. Schwingenschlögl, *ACS Appl. Mater. Interfaces*, 2020, **12**, 30731.
54 A. Mallah, M. Debbichi, M. H. Dhaou and B. Bellakhdhar, *Crystals*, 2023, **13**, 126.
55 K. Liu, Q. Yan, M. Chen, W. Fan, Y. Sun, J. Suh, D. Fu, S. Lee, J. Zhou, S. Tongay, J. Ji, J. B. Neaton and J. Wu, *Nano Lett.*, 2014, **14**, 5097–5103.
56 O. Leenaerts, H. Peelaers, A. D. Hernández-Nieves, B. Partoens and F. M. Peeters, *Phys. Rev. B:Condens. Matter Mater. Phys.*, 2010, **82**, 195436.
57 Dimple, N. Jena, A. Rawat, R. Ahammed, M. K. Mohanta and A. De Sarkar, *J. Mater. Chem. A*, 2018, **6**, 24885–24898.
58 C.-F. Fu, J. Sun, Q. Luo, X. Li, W. Hu and J. Yang, *Nano Lett.*, 2018, **18**, 6312–6317.
59 W. Wan, S. Zhao, Y. Ge and Y. Liu, *J. Phys.:Condens. Matter*, 2019, **31**, 435501.
60 S.-D. Guo, W.-Q. Mu, Y.-T. Zhu, R.-Y. Han and W.-C. Ren, *J. Mater. Chem. C*, 2021, **9**, 2464–2473.
61 N. N. Hieu, H. V. Phuc, A. I. Kartamyshev and T. V. Vu, *Phys. Rev. B*, 2022, **105**, 075402.
62 Z. Gao, X. He, W. Li, Y. He and K. Xiong, *Dalton Trans.*, 2023, **52**, 8322–8331.
63 N. T. Hiep, C. Q. Nguyen and N. N. Hieu, *Appl. Phys. Lett.*, 2023, **123**, 092102.
64 S.-Z. Huang, C.-G. Fang, Q.-Y. Feng, B.-Y. Wang, H.-D. Yang, B. Li, X. Xiang, X.-T. Zu and H.-X. Deng, *Langmuir*, 2023, **39**, 2719–2728.
65 T. V. Vu, B. D. Hoi, A. I. Kartamyshev and N. N. Hieu, *J. Appl. Phys.*, 2024, **135**, 074301.